Heat exchanger design based on earthen materials

Chafea Bouchenna, Florian Huchet, Carl Aramiou, Erwan Hamard, Laurédan Le Guen, Jean-Marc Paul

Energy, 227 (2021)
DOI: 10.1016/j.energy.2021.120385

Heat exchanger design based on earthen materials

Keywords: Thermal energy storage - Packed bed - Free cooling - Data center

Chafea BOUCHENNA[1], Florian HUCHET[1], Carl ARAMIOU[1], Erwan HAMARD[1], Laurédan LE GUEN[1], Jean Marc PAUL[1]

[1] *MAST-GPEM, Univ. Gustave Eiffel, IFSTTAR, F-44344 Bouguenais, France*

Abstract

We propose herein the design of a heat exchanger based on clay materials in order to reduce the energy consumed due to data center cooling. Our Thermal Energy Storage (TES) system is to be placed upstream of the CRAC (Computer Room Air Conditioner) unit. A direct contact heat exchanger is thereby built as a vertical packed bed, composed of earthen spheres whose imposed heating/cooling cycles comply with ASHRAE (American Society of Heating, Refrigerating and Air-Conditioning Engineers) standards. A raw earthen material has been chosen owing to its hygrothermal characteristics, which are recognized as relevant for indoor thermal regulation, in addition to a low embodied energy required for manufacturing. Results show that the pore Reynolds number and sphere diameter exert significant effects on the energy buffering capacity. A simple relationship is thus proposed to link the mass-specific power of the energy storage system, the internal heat exchanger architecture and the pore Reynolds number for purposes of designing raw earth bricks at an elevated scale.

1. Introduction

TES from mineral materials (e.g. sand, rocks, bricks, concrete) has been of great research interest for quite some time [1], especially in the area of solar collector applications such as rock bed containers [2]. The low specific heat values of these tested materials have however reduced their attractiveness by virtue of occupying large volumes under actual working conditions. Recent advances in civil engineering materials and microprocess engineering could

spark renewed interest in such technologies. We are therefore proposing in this context to study earthen materials, which are recognized for the magnitude of their permeability to water vapor and which, until now, had never been considered for use in gas/solid packed bed storage application [3]. Their energy storage capability will be evaluated within the framework of the data center cooling problem.

In light of the upcoming digital growth tied to the IoT (Internet of Things), the future of data centers is today confronted with the challenge of maintaining annual steady operations while reducing energy consumption. Consequently, the indoor thermal regulation of such buildings has now become a priority R&D issue. In 2013, the energy cost of this infrastructure accounted for up to 1.3% of the world's electricity consumption [4]. It is widely accepted that the energy consumption of a data center is distributed as follows: 40% for the IT equipment (server, processor, storage), 20% for the power system supply (battery management, building switchgear, lighting), and 40% for the cooling system. The green grid group has therefore proposed an energy efficiency criterion, PUE (Power Usage Effectiveness), based on the ratio of the sum of all powers, P, *vs*. IT power, P_{IT} [5]. More recently, this PUE criterion has been reformulated to take into account the Energy Reuse Power, P_{reuse}, according to following relationship:

$$ERE = PUE - \frac{P_{reuse}}{P_{IT}} = \frac{P_{cooling}+P_{power}+P_{lighting}+P_{IT}-P_{reuse}}{P_{IT}} \quad (1)$$

with ERE denoting Energy Reuse Effectiveness [6].

A review [7] performed in 2017 on 100 data centers showed that the PUE values ranged between 1.33 and 3.85, with an average estimated at 2.13. This value underscores the need to deliver twice the required power strictly devoted to the IT equipment, thus demonstrating the

anticipated energy improvements necessary for such buildings. Active cooling from CRAC (Computer Room Air Conditioner) units, based on mechanical vapor compression refrigeration, has been extensively implemented in order to respect ASHRAE's hygrothermal standard [8].

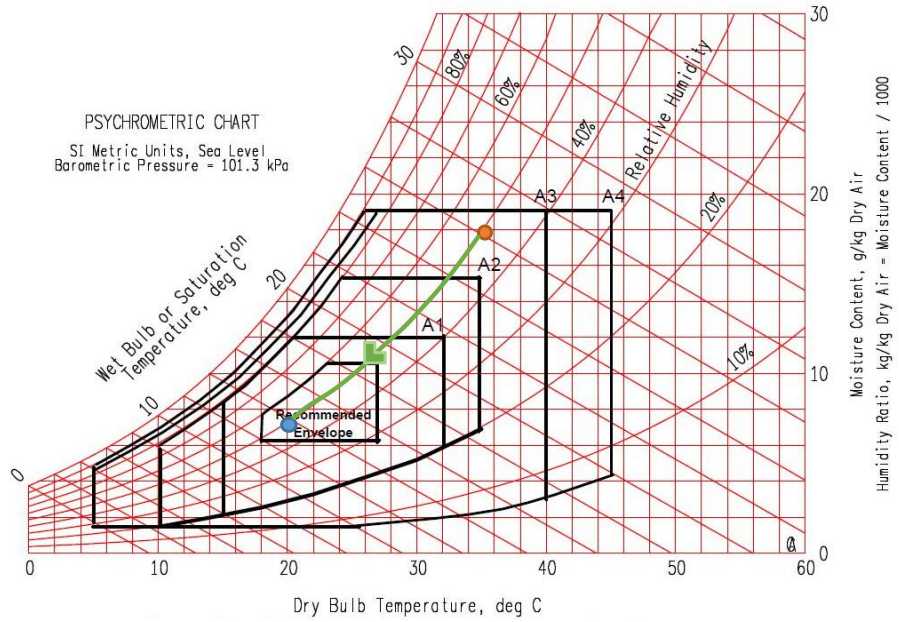

Figure 1: *ASHRAE environmental classifications for data centers [8] - the climatic condition for the present work is depicted on the green line between the orange and blue circles.*

A data center designation is intended to cover several ASHRAE standard classes, as shown in Figure 1. A1 and A2 classes recommend a dry-bulb temperature ranging from 15° to 32°C for a humidity rate lying between 20% and 80%, as expected in a European region. A3 and A4 classes have been expanded to include the tropical regions. Given this context, several passive cooling techniques have emerged under the broad banner of "free cooling" and have become widespread nowadays for data center facilities. Based on the use of a natural energy source for cooling, these techniques can be categorized into several domains [9], namely: air-side free cooling relying on outside air temperature, water-side free cooling, and heat pipe systems. Despite its lower energy performance, the first category remains much more extensive within the data center community thanks to its simplicity; moreover, considerable research has been

devoted to studying airflow distribution in computer rooms [10]. The second category (water-side free cooling) is dependent on freshwater storage located near the data center or underground, hence at a significant economic cost and involving technical complexity. The third category (heat pipe systems) has recently attracted widespread interest due to its ability to transfer heat in the presence of small temperature differences without requiring any external energy. This latter technology is capable of inserting cold energy storage [11] or a new thermodynamic cycle of evaporation/condensation by means of refrigerant liquid, thus promoting heat waste reuse at the district scale [12].

The motivation behind this work centers around the warm period, which is becoming more prevalent, thus causing CRAC unit overconsumption peaks and shortening the free cooling periods. In order to maintain, or perhaps extend, the free cooling periods, the present solution proposes positioning a direct contact heat exchanger built using raw earth bricks upstream of the CRAC unit. Air circulation through the exchanger can then potentially satisfy the two configurations sketched in Figure 2: (i) outdoor air is preferred to reach the temperature setting; and (ii) a portion of the return air discharged from the computer room is reused.

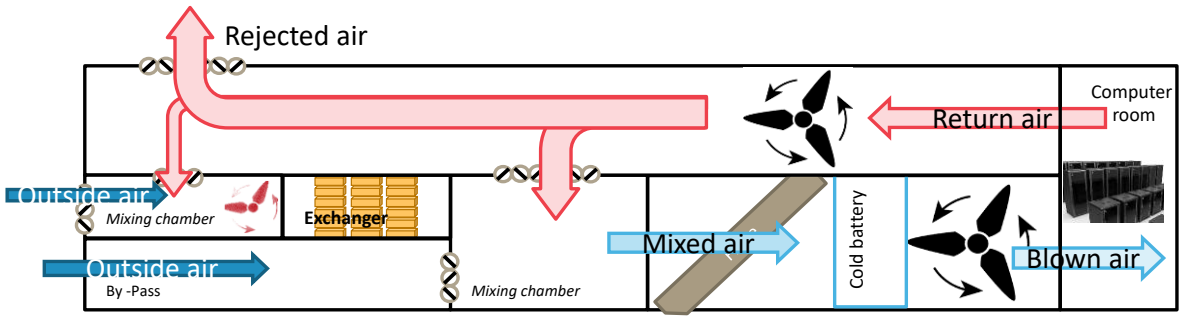

Figure 2: *Positioning of the present research work - regardless of the cooling system configuration, a raw earth block plays the role of cold storage system, thereby guaranteeing a decrease in the CRAC power during the active cooling period or else extending the passive cooling period.*

A raw earthen material composed of sands and clay has been chosen herein because of its high hygrothermal inertia and permeability to water vapor, both of which are relevant to regulating indoor thermal comfort [13]. On the other hand, the embodied energy of such materials is recognized as being low [14] throughout their manufacturing stages, from extraction to production and all the way to their reuse.

Forced convection through such a double-porosity medium remains an active field of research, especially in an effort to determine suitable materials for an energy storage solution within the scope of renewable energy deployment. A packed bed of earth bead materials is a relevant candidate for a standard benchmark system intended to:

(i) experimentally explore the Local Thermal Non-Equilibrium (LTNE) between the fluid and solid phases at a significant scale difference between external porosity and microporosity;

(ii) extend to other TES applications involving subsoil materials.

The novelty of this experimental research lies in assessing the storage energies of a direct contact heat exchanger composed of raw earth spheres under controlled aero-thermal conditions suited to scaling-up. The charging/discharging cycles follow the green line highlighted in the ASHRAE Standard (Fig. 1). The present paper is organized in four sections. Following this introduction, Section 2 will be devoted to the materials and methods, including the flow loop and materials preparation. Results will be discussed in the third section, while a number of conclusions and an outlook will be drawn in Section 4.

2. Materials and methods

2.1 Packed bed design

The laboratory-scale heat exchanger is composed of a vertical packed bed of spherical raw earthen materials, placed in a Plexiglas cylindrical container with a height H = 270 mm and diameter D = 140 mm. Several bed compactness values were studied by varying the size of the raw earth spheres. Three sphere diameters, d_s, were designed such that: $d_s = \frac{D}{3.11}, \frac{D}{4}, and\ \frac{D}{9.3}$. The preparation of raw earth spheres encompasses several steps, as illustrated in Figure 3. The solid phase is composed of a raw earthen material originating in Brittany (80%) and sand particles (20%) 4 mm in diameter mixed with tap water featuring a mass fraction $\frac{m_{water}}{m_{solid}} = 0.36$. The resulting plastic materials exhibit sufficiently soft behavior to be deposited into spherical molds of diameters 15 mm, 32 mm and 45 mm. These molds were maintained at 40°C in an oven until the mass stabilized before demolding. This drying yield temperature is necessary to conserve the hygrothermal properties of the original materials. In the hardened state, both the solid density, ρ_s, and specific heat, Cp_s, were measured under the working temperature of the heat exchanger as seen in Table 1.

Table 1: Thermophysical parameters of the fluid and solid phases.

ρ_s (kg.m^{-3})	1,792.9
ρ_f (kg.m^{-3})	1.2
Cp_s (J.Kg^{-1}.K^{-1})	840
Cp_f (J.Kg^{-1}.K^{-1})	1,009

The packed bed of mass, m, was treated using a standard pore model [15] at the particle scale of characteristic length, d_s; its structural parameters are listed in Table 2, depending on the specific surface area, a_v, and external porosity, ε, as given by:

$$\varepsilon = 1 - \left(\frac{m}{\rho_s}\right) / \left(\frac{\pi D^2}{4} H\right) \quad (2)$$

Thus, the pore diameter, d_p, can be calculated according to the following relationship:

$$d_p = \frac{4\varepsilon}{a_v\,(1-\varepsilon)}, \text{ with } a_v = \frac{6}{d_s} \quad (3)$$

The pore Reynolds number, Re_p, is given by:

$$Re_p = U_p d_p / \nu_f \quad (4)$$

with $U_p = \frac{U_s\,\tau}{\varepsilon}$ being dependent on the superficial velocity, U_s, as calculated in an empty cylinder, and tortuosity, τ, equal to $\sqrt{2}$ for the spherical particles, as suggested in [16].

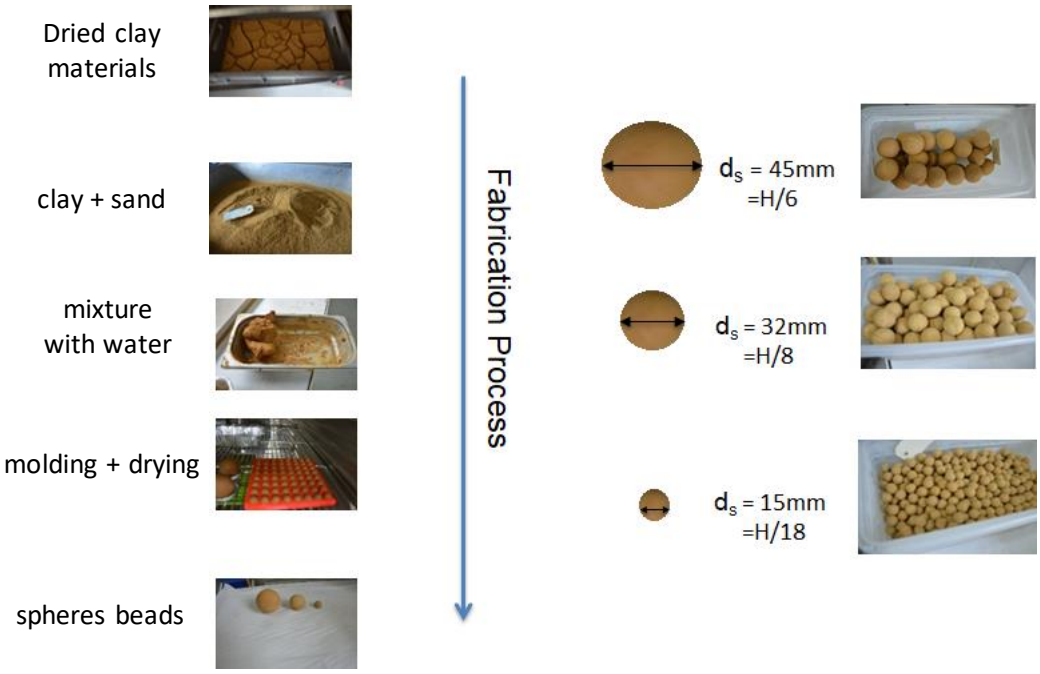

Figure 3: *Manufacturing of the packed bed of beads.*

The earth spheres have sustained slight shrinkage, hence explaining the difference between mold size and actual bead size. The uncertainties in the pore diameters and sphere diameters, as reported in Table 2, have thus been assessed by means of image analysis (i.e. Image J software). These relative uncertainties act on the pore Reynolds number uncertainties such that:

$$\frac{|\Delta Re_p|}{Re_p} = \left|\frac{\Delta U_p}{U_p}\right| + \left|\frac{\Delta d_p}{d_p}\right| \quad (5)$$

It should be noted that the large size of particles plays a significant role on the structural parameters of the packed bed exhibiting the lightest weight and the highest external porosity as reported in Table 2.

Table 2: Structural parameters of the packed bed.

D/d_s	3.11	4	9.3
Packed bed mass, m (kg)	4.28	4.29	4.72
Sphere diameter, d_s (mm)	44.7 ± 0.7%	30.6 ± 2.27%	14.7 ± 2.32%
a_v (m^{-1})	134	196	408
ε	0.42	0.42	0.36
d_p (mm)	21.5 ± 29%	14.6 ± 26%	5.5 ± 32%
$Re_p \pm \|\Delta Re_p\|/Re_p$	[833 - 4241] ± 31%	[589 - 3100] ± 28%	[252 - 1334] ± 34%

2.2 Flow rig

The mass airflow rates are controlled at room temperature by using a fan to set the cooling cycles. For the heating cycles, a thermal cleaner is able to control the mixing-cup temperature at the entrance to the packed bed. One divergent inlet and one convergent outlet, both made of PLA (polyactic acid) by 3D printing (Ultimaker), were connected to two straight tubes downstream and upstream respectively of the experimental system. A honeycomb sheet, with a mesh size equal to 4 mm, ensured a plug flow at the entrance to the packed bed.

The sensor-fitted flow rig is diagrammed in Figure 4; it is composed of a set of temperature probes (K-thermocouples) located between the inlet and the outlet to measure the fluid and solid phases. For each compactness value, three probes were immersed into the beads during molding. A square porthole in Zn/Se, with a side length equal to 10 cm, was devoted to

temperature control by means of infrared imaging. The velocity profiles were assessed from two L-Pitot tubes positioned upstream and downstream of the exchanger in order to control the mass flow rates; they were inserted into an inlet tube of diameter D_t equal to 44 mm at the tube length location that respected the turbulent flow developed at a distance 10 D_t downstream of the fan position.

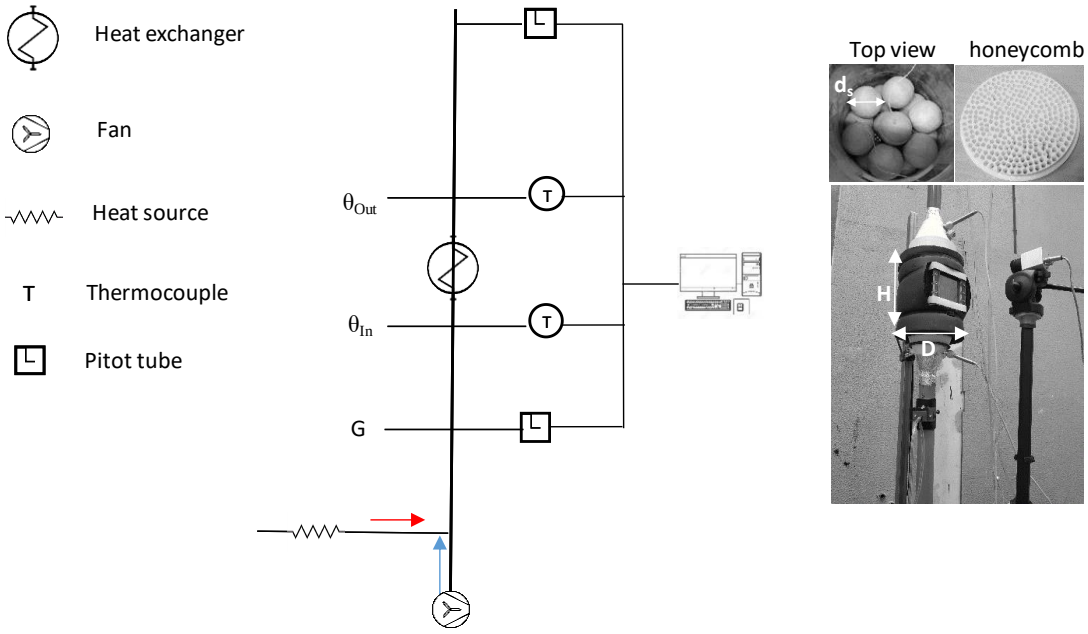

Figure 4: Experimental set-up of the direct contact heat exchanger - left) thermal flow loop configuration; right) pictures of the experimental set-up, including the smallest D/d_s ratio.

For each packed bed compactness value, a wide range of Reynolds numbers was imposed at the inlet. A few velocity profiles are shown in Figure 5; these profiles, measured at the inlet, correspond to a turbulent flow regime in a straight duct, as compared to the Nikuradse relationship [17], such that:

$$V(r) = V_{max} \times (1 - r/R)^{1/n} \text{ with } n = 7 \quad (6)$$

The average velocity is therefore calculated by means of integration according to a Simpson method along the duct cross-section, which will be substituted in the remaining hydrodynamic parameters assessment, i.e. the mass flow rate and Reynolds number.

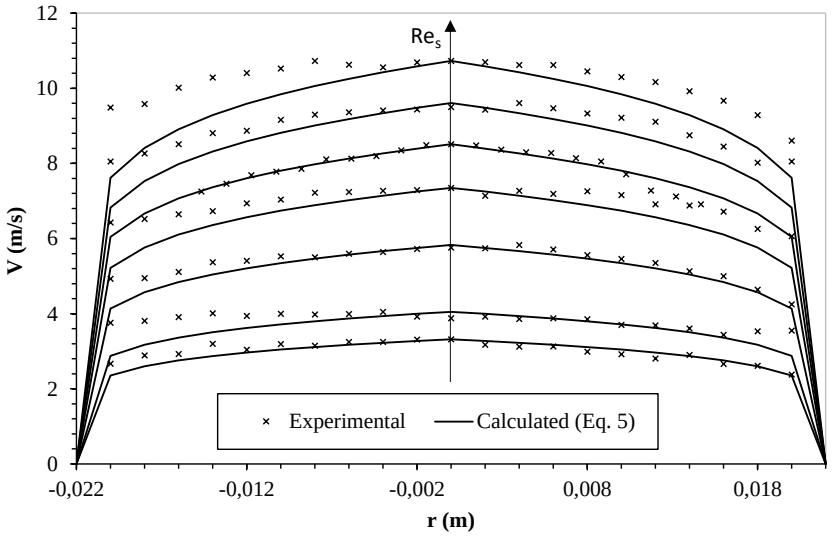

Figure 5: Velocity profiles obtained at the inlet tube,
and comparison with fully developed turbulent flow profiles obtained from Equation (5).

The heat exchanger needs to be designed for scaling-up. The pore scale corresponds to an elementary brick of earth, while the container scale corresponds to the total exchanger volume. Therefore, the superficial Reynolds number is based on the superficial velocity, U_s, such that:

$$Re_s = \frac{\rho_f U_s D}{\mu_f} \tag{7}$$

where D is the container diameter, ρ_f the fluid density, and μ_f the dynamic viscosity of the fluid.

Figure 6 (left) shows the effect of the characteristic length of the packed bed on the pore Reynolds numbers. At an identical imposed velocity, corresponding to a given superficial Reynolds number, Re_s, various flow regimes are identified through the packed bed; this result

is due to the pore cross-section varying with sphere diameter. The dependence of Re_p on Re_s differs according to sphere diameter. The slope is governed by a parameter α correlated with d_s. From relationships (2) and (3) above, the pore Reynolds number can easily be computed from the superficial Re_s based solely on the architectural parameters of the packed bed, i.e.:

$$Re_p = \alpha Re_s \tag{8}$$

with

$$\alpha = \frac{2}{3}\frac{\tau}{(1-\varepsilon)}\frac{d_s}{D} \tag{9}$$

Since the elementary sphere is small, the pore diameter has been reduced as has the pore Reynolds number. An Ergun-type equation [18] is recognized as suitable to accurately estimate the pressure drop through the packed beds of spherical particles within a wide range of applicability ($3.8 < D/d_s < 40$):

$$\frac{\Delta P}{H} = A.\left(\frac{\rho_f.{U_s}^2}{d_s}\right)\left(\frac{(1-\varepsilon)}{\varepsilon^3}\right)\left(\frac{D}{d_s}\right)^{0.2}\left[1000Re_{d_s}^{-1} + 60Re_{d_s}^{-0.5} + 12\right] \tag{10}$$

with A= 0.061 and $Re_{d_s} = \frac{\rho_f U_s\, d_s}{\mu_f}$.

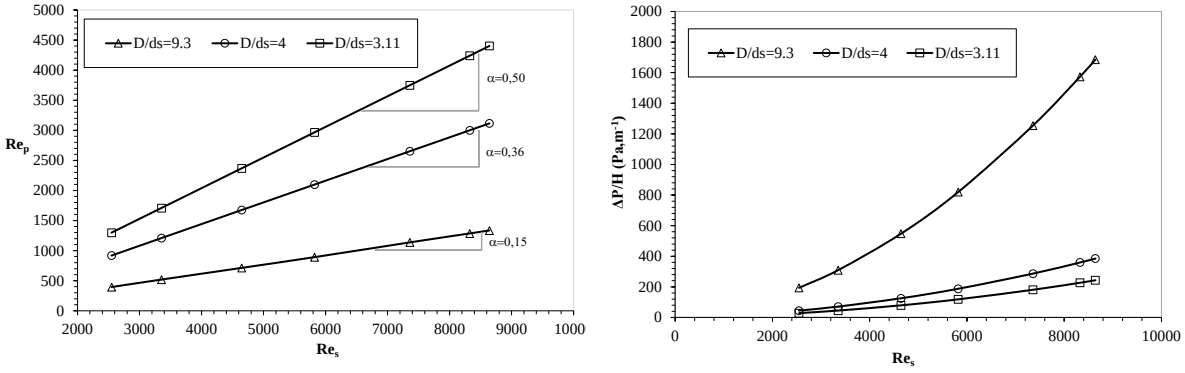

Figure 6: left) Superficial Reynolds numbers *vs.* pore Reynolds numbers correlated with the α parameter; **right)** Dependence of pressure drop on the Re_s obtained from Equation (10) for various spherical particle diameter values.

Figure 6 (right) illustrates the quadratic dependence of the pressure drop across the packed bed for various Re_s number values; it can be observed that the greater pressure drops occur at the highest Re_s values and for the smallest particles. The rate of increase of the pressure drop is expected to be negligible within the range of the Re_s values investigated herein.

3. Results and Discussion

As mentioned above, the designed heat exchanger targets data center cooling with respect to ASHRAE Classes A1 and A2. Consequently, we have opted to introduce an initial cycle of heat accumulation by varying the temperature from 20°C to 35°C at a constant 50% humidity rate, followed by a second cycle by switching the inlet cooling temperature at close to 20°C. To study the effect of the internal heat exchanger architecture and airflow rates, we have varied the sphere diameters and superficial Reynolds number. During the first (charging) period, hot air flows through the packed bed in a forced convection regime over the earth bead surface. Note that heat conduction at the contact points between particles also acts upon the transfer phenomenon. During the second (discharging) period, the incoming cooled air is gradually heated from the accumulated energy into the earth beads. Charging and discharging cycles are fully achieved once the overall earthen materials equal the incoming fluid. Figure 7 presents the dimensionless temperature θ^* variation, defined according to the charging cycle as:

$$\theta^*_{HTF}(t^*) = \frac{\theta(t^*) - \theta^{CTF}_{In}(t^* \approx 1)}{\overline{\theta^{HTF}_{In}} - \theta^{CTF}_{In}(t^* \approx 1)} \tag{11}$$

And according to the discharging cycle as:

$$\theta^*_{CTF}(t^*) = \left| \frac{\theta(t^*) - \theta^{HTF}_{In}(t^* \approx 1)}{\overline{\theta^{CTF}_{In}} - \theta^{HTF}_{In}(t^* \approx 1)} \right| \tag{12}$$

with the dimensionless time t^* defined such that:

$$t^* = \frac{t}{t_f} \tag{13}$$

The cycle time t_f is defined as the time at which the outlet temperature of air leaving the exchanger is constant and equal to approx. 10% of the incoming air temperature, i.e.:

$$\frac{\theta_{In}^{HTF}(t=t_f)-\theta_{Out}^{HTF}(t=t_f)}{\overline{\theta_{In}^{HTF}}-\theta_{Out}^{HTF}(t=0)} \cong 0.1 \text{ and } \frac{\theta_{Out}^{CTF}(t=t_f)-\theta_{In}^{CTF}(t=t_f)}{\theta_{Out}^{CTF}(t=0)-\overline{\theta_{In}^{CTF}}} \cong 0.1 \tag{14, 15}$$

During a charging cycle, the time variation of the dimensionless inlet temperature of the Heat Thermal Fluid (HTF) is constantly close to a value of 1, while the dimensionless temperature inside the earth beads, positioned respectively at z = 0, z = H/2 and z = H, is gradually increasing. These results show that the earth beads accomplish the role of energy storage whenever a large difference between inlet and outlet air temperature arises. This energy buffer capability is lost when this difference is reduced to a minimum, corresponding to a dimensionless time equal to 1. This time in turn corresponds to the end of the LTNE period. During a discharging cycle, the inlet flow is fixed at ambient temperature θ_{In}^{CTF} as the Cooling Thermal Fluid (CTF). The outgoing air temperature gradually decreases as long as the energy accumulated in the earth beads is being redistributed into the fluid phase. The energy stored during the first loading is thus restored during unloading. The solid phase and fluid phase temperatures systematically remain far from the equilibrium regardless of the measurement position for a given period.

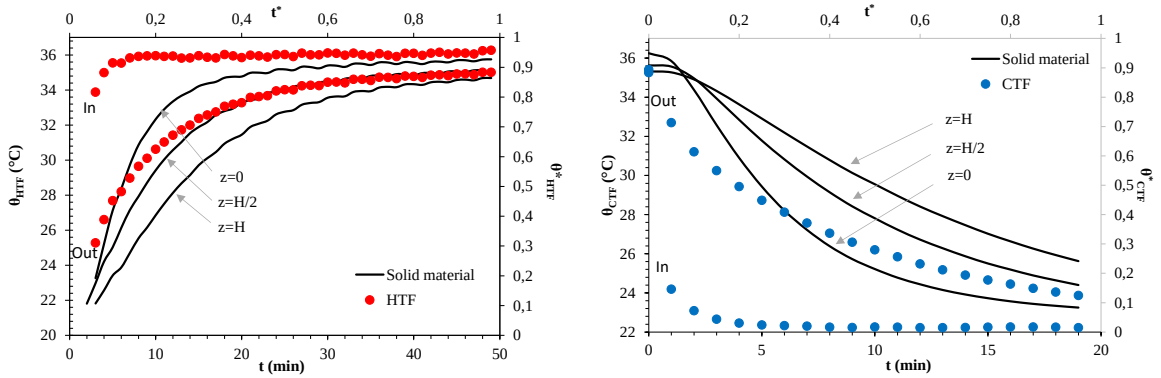

Figure 7: Temperature variation *vs.* time during successive charging cycles (left) and discharging cycles (right) $\{D/d_s = 3.11,\ \mathrm{G} = 0.0168\ \mathrm{kg/s}$ and $\mathrm{Re}_p = 6708\}$.

The effect of raw earth sphere size on thermal energy stored/released into the heat exchanger during heating/cooling cycles is calculated according to a time-averaged thermal balance:

$$Q = \int_0^{t_f} G.C_{p_f}.(\overline{\theta_{in}} - \theta_{out}(t)).dt \tag{16}$$

Over more than 30 cycles performed on the granular assembly, no single cycle has given rise to strain rate damage or a defect in heat accumulation as the experimental campaign progressed. Three typical cumulative energy hysteresis effects are reported in Figure 8, which shows the relative increases in their absolute magnitude as sphere size decreases. The main parameters controlling storage capability are the full earth mass and specific surface area of the packed bed. In the present case, the earth masses are similar between the various packed bed arrangements, except for those containing the smallest beads.

To pursue these results even further, we are proposing to reduce the present problem by introducing a mass-specific power that represents the thermal power of the exchanger, i.e.:

$$SP = \frac{P}{m} \tag{17}$$

with P being the thermal power of the heat exchanger, as given by:

$$P = \frac{Q}{t_f} \tag{18}$$

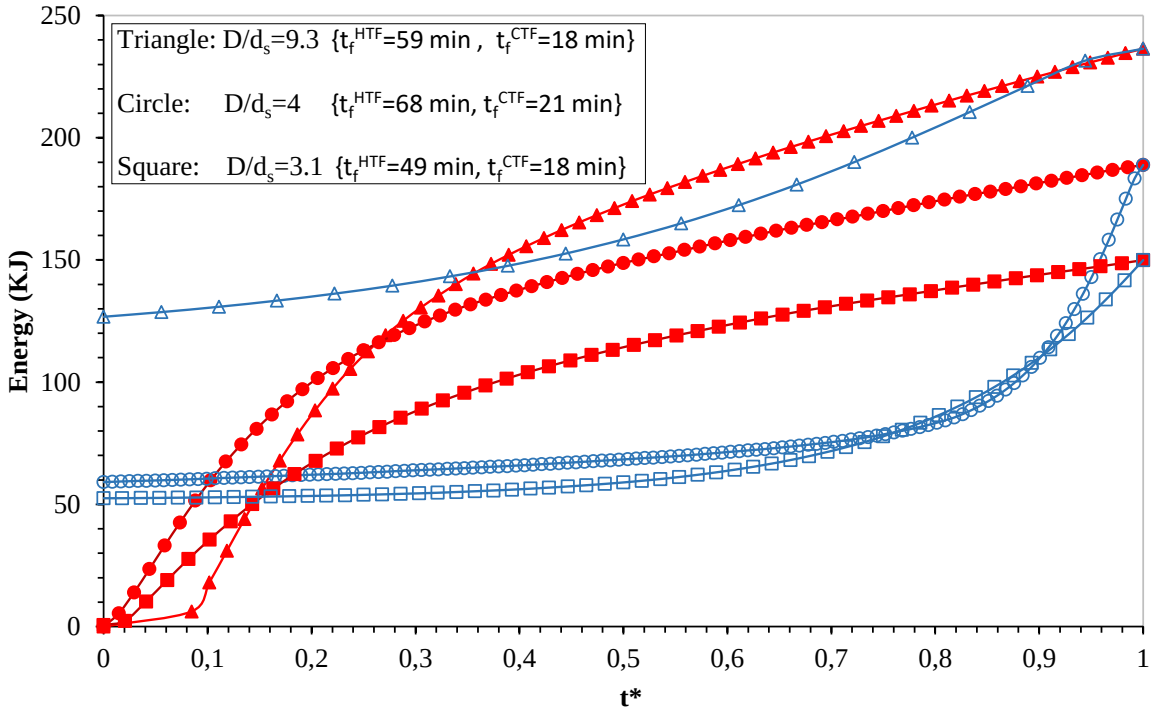

Figure 8: Energy hysteresis occurring during two successive cycles of loading (full symbol, for Re_s=8,642) and unloading (empty symbol, for Re_s=7,880), for different sphere sizes.

Figure 9 displays the mass-specific power, which increases with Re_p regardless of the sphere size. Moreover, the curve slopes tend to increase as sphere diameter becomes smaller. The specific surface area, as indicated in Table 2, is greater for smaller spheres, thus giving rise to improved heat exchange; mass power is higher in the case of the smallest earth bead size.

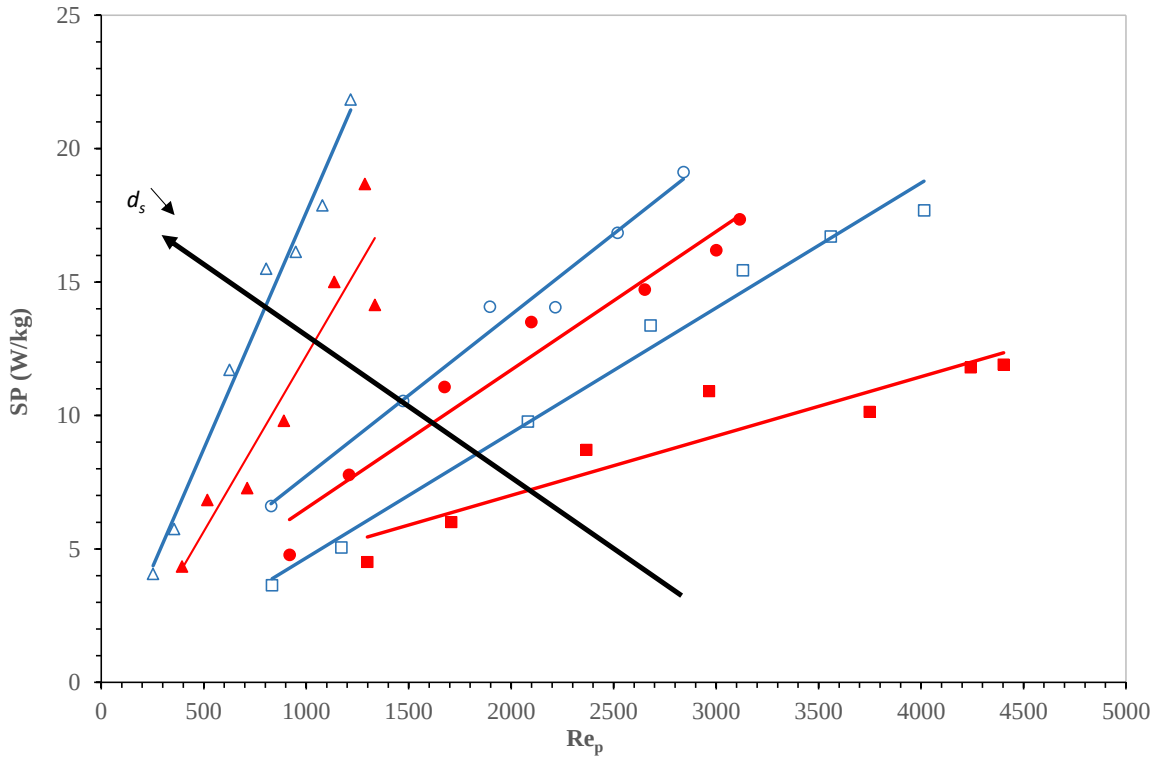

Figure 9: Mass-specific power *vs*. pore Reynolds number for the various packed bed arrangements Full symbol: Charging cycle - Empty symbol: Discharging cycle - Square: $D/d_s = 3.11$ - Circle: $D/d_s = 4$ - Triangle: $D/d_s = 9.3$.

From these overall results, a relationship can be computed by multiplying the mass power by a structural parameter based on the ratio of container height to sphere diameter. Figure 10 depicts a cloud of points corresponding to the mass-specific power of the charging/discharging cycles, for different bead sizes within the overall range of pore Reynolds numbers corresponding to the transient $(200 > Re_p > 1100)$ and turbulent $(Re_p > 1100)$ flow regimes known in porous matrix [19]. These experimental results are quite well represented by a power law with a Mean Relative Error, ERM, equal to 17%, according to:

$$\left(\frac{D}{d_s}\right)^{-1}.SP = \delta.Re_p^{\beta} \tag{19}$$

with $\delta = 0.026\ W/kg$ and $\beta \cong 0.91$.

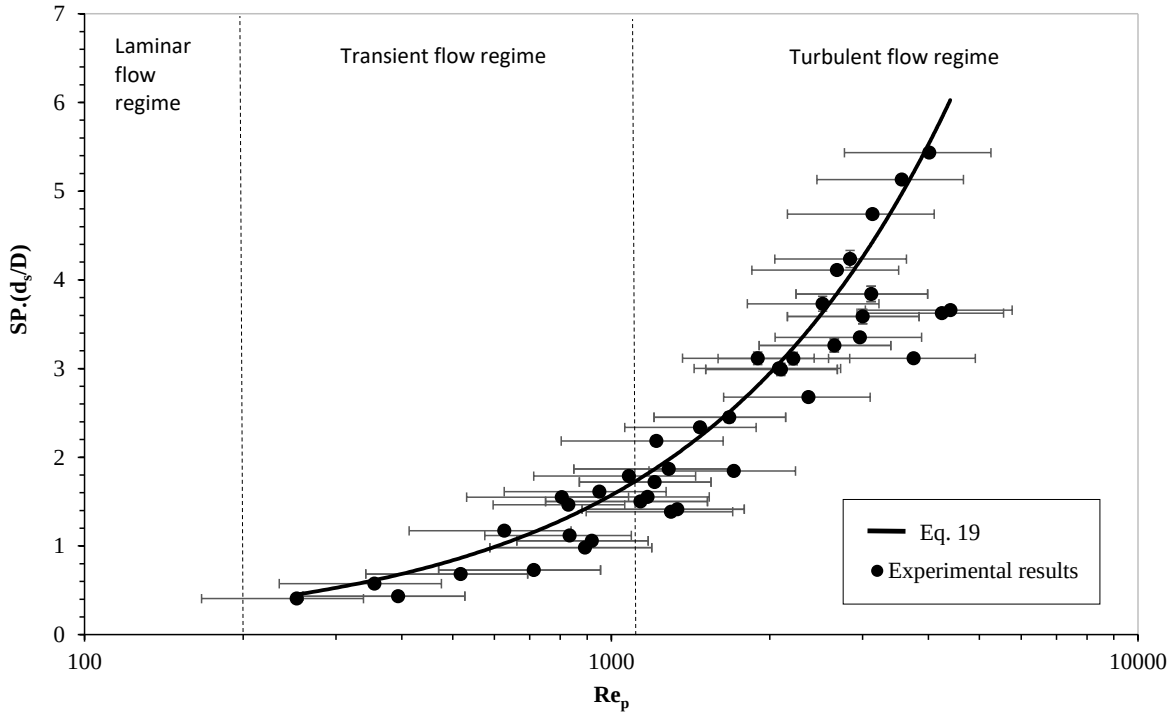

Figure 10: Mass-specific power multiplied by the structural parameter of the packed bed vs. the pore Reynolds number - experimental results and uncertainties are compared with Eq. (19).

The β parameter does not correspond to any exponent found in the heat/mass transfer literature [20] since the correlation is not dimensionless. However, such a correlation has the advantage of enabling scaling-up by taking into account the TES capacity (~*SP*), the structural parameter (~d_s/D) and the aeraulic performance (~Re_p).

4. Conclusion

The present work, performed at the laboratory scale, has been intended to design a heat exchanger based on earthen materials using TES technology for its installation into a data center building. A cylindrical packed bed has been produced from calibrated earth spheres prior to their processing and molding. Heat and Cooling Thermal Fluids (HTF/CTF), along with

ventilation controlled by means of a sensor-fitted flow rig, served to characterize the energy buffering capacity of such a system. The key points of this research work are detailed below:

- Three compactness values of the packed bed have been studied by varying the sphere diameters at a constant cylindrical diameter.
- Re_s and Re_p have been chosen as the relevant parameters of TES system scaling-up.
- The pressure drop reaches a maximum close to 2 kPa/m for the smallest sphere size at Re_s ~ 8,500. The ratio between Re_p and Re_s is governed by the parameter α, which evolved in sync with the packed bed compactness level.
- The measured thermal kinetics during both the loading (HTF) and unloading (CTF) stages are governed by the final time, t_f, which corresponds to the end of the LTNE period.
- The internal architecture of the packed bed governs the loading/unloading kinetics; the the highest mass-specific powers are reached in discharging phase ($SP^{CTF}_{D/d_s=9.3}$~22 kW/t ; $SP^{CTF}_{D/d_s=4}$~19 kW/t ; $SP^{CTF}_{D/d_s=3.11}$~17 kW/t) and the optimum result corresponds to the smallest size of sphere.
- A relationship (Eq. 19) has been proposed to predict the mass-specific power from a structural parameter of the packed bed (D/d_s) and the pore Reynolds number.

The two main directions of future research are currently being explored:

- the thermal hysteresis behavior with respect to both the material properties and process parameters;
- the role of microporosity in TES performance

Nomenclature

Abbreviations

ASHRAE – American Society of Heating, Refrigerating and Air-Conditioning Engineers

CRAC – Computer Room Air Conditioner

CTF – Cooling Thermal Fluid

CFD – Computational Fluid Dynamics

ERE – Energy Reuse Power

HTF – Heat Thermal Fluid

In – Inlet

IoT – Internet of Things

IT – Information Technologies

Out – Outlet

PUE – Power Usage Effectiveness

R&D – Research and Development

TES – Thermal Energy Storage

Symbols

Cp_f – fluid specific heat, [J.kg^{-1}.K^{-1}]

Cp_s – solid specific heat, [J.kg^{-1}.K^{-1}]

D – inner diameter of the container, [m]

d_s – sphere diameter, [m]

d_p – pore diameter, [m]

G – mass airflow rate, [kg.s^{-1}]

H – height of container, [m]

m– full earth mass, [kg]

P – power, [W]

Q – energy, [J]

r – coordinate, [m]

R – duct radius, [m]

SP – mass-specific power, [W.kg^{-1}]

Re_{d_s} – particle Reynolds number, [–]

Re_p – pore Reynolds number, [–]

Re_s – superficial Reynolds number, [–]

t – time, [s]

t_f – final time, [s]

t^*– dimensionless time, [–]

U_p – pore velocity, [m.s^{-1}]

U_s – superficial velocity [m.s^{-1}]

V – velocity in straight duct, [m.s^{-1}]

V_{max} – maximum velocity, [m.s^{-1}]

f – fluid

s – solid

Greek symbols

α – slope coefficient, [–]

ΔP – pressure drop, [Pa]

ε – external porosity, [–]

μ – dynamic viscosity, [Pa·s]

ρ – fluid density, [kg.m^{-3}]

θ – temperature, [°C]

θ^* – dimensionless temperature, [–]

τ- tortuosity, [–]

Acknowledgments: This work was funded by the French Agency for Ecological Transition (ADEME) under the project name "*Projet Data Centre Eco-Responsable*" (No. 1704C0008). We thank Samuel Dugelay (Makjo) and Nicolas Miceli (APL Data Center) for our fruitful discussions.

References

[1] Boisdet A., Peube J.L., Blay D. Stockage thermique en milieu poreux granulaire. Revue de Physique Appliquee, 1982 ;17(9) :591-594. 10.1051/rphysap:01982001709059100. jpa-00245036

[2] Dang Vu C., Delcambre B. Etude expérimentale et modélisation d'un stockage thermique de longue durée en lit de cailloux enterré, couplé à des capteurs solaires à air. Revue de Physique Appliquee 1987 ; 22 (7):487-503. 10.1051/rphysap:01987002207048700. jpa-00245565

[3] Esence T., Bruch A., Molina S., Stutz B., Fourmigué J.F. A review on experience feedback and numerical modelling of packed-bed thermal energy storage systems. Solar Energy 2017;153:628-654

[4] Nadjahi C, Louahlia H, Lemasson S. A review of thermal management and innovative cooling strategies for datacenter. Sustainable Computing: Informatics and Systems 2018;19:14-28.

[5] GREEN GRID METRICS: Describing data center Power Efficiency. Green Grid WP #1, 2007

[6] Tschudi B, Berkeley L. Ere: a metric for measuring the benefit of reuse energy from a datacenter. Star (2010)

[7] Ni J., Bai X., A review of air conditioning energy performance in datacenters, Renewable and Sustainable Energy Reviews 2017;67:625-640.

[8] ASHRAE whitepaper. Thermal guidelines for data processing environments —expanded datacenter classes an usage guidance, Technical Committee (TC) 9.9, ASHRAE;2011

[9] Lu H, Zhang Z, Yang L. A review on airflow distribution and management in datacenter, Energy and Buildings 2018;179:264-277.

[10] Zhang H, Shao S, Xu H, Zou H, Tian C. Free cooling of datacenters: A review. Renewable an Sustainable Energy Reviews 2014;35:171-182.

[11] Singh R, Mochizuki M, Mashiko K, Nguyen T. Heat pipe based cold energy storage systems for datacenter energy conservation. Energy 2011;36:2802:11.

[12] He Z, Ding T., Liu Y, Li Z. Analysis of a district heating system using waste heat in a distributed cooling datacenter. Applied Thermal Energy 2018;141:1131-1140.

[13] Soudani L, Woloszyn M, Fabbri A, Morel J, Grillet A. Energy evaluation of rammed earth wall using long term in-situ measurement. Solar Energy 2017;141:70-80.

[14] Van Damme H., Houben H. Earth concrete. Stabilization revisited. Cement and Concrete Research 2018;114:90-102.

[15] Huchet, F., Roquet, N. & Cazacliu, B. Advection-dispersive Mechanism of electrolyte species in porous matrix. Transport in Porous Media 2014;104:299-313.

[16] Carman, P.C. Fluid flow through a granular bed. Trans. Inst. Chem. Eng. 1937;15:150.

[17] Schlichting, Hermann. *Boundary layer theory*. Vol. 960. New York: McGraw-Hill, 1960.

[18] Montillet A., Akkari E., Comiti J. About a correlating equation for predicting pressure drops through packed beds of spheres in a large range of Reynolds numbers. Chemical Engineering and Processing: Process Intensification 2007;46(4):329-333.

[19] Huchet F., Comiti J., Tihon J., Montillet A., Legentilhomme P. Electrodiffusion diagnostics of the flow and mass transfer inside a network of crossing minichannels. Journal of Applied Electrochemistry 2007;37(1):49-55.

[20] Nield, D.A., Bejan A., Convection in porous media, New York, Springer 2006.